^{18}F-Labeled Magnetic-Upconversion Nanophosphors *via* Rare-Earth Cation-Assisted Ligand Assembly

Qian Liu,[†] Yun Sun,[†] Chenguang Li,[†] Jing Zhou,[†] Chunyan Li,[†] Tianshe Yang,[†] Xianzhong Zhang,[‡] Tao Yi,[†,*] Dongmei Wu,[§] and Fuyou Li[†,*]

[†]Joint Center of Biomedical Imaging (BMI) of Department of Chemistry & Institute of Biomedical Science & Cancer Hospital, and Advanced Materials Laboratory, Fudan University, 200433, People's Republic of China, [‡]Key Laboratory of Radiopharmaceuticals, Ministry of Education, College of Chemistry, Beijing Normal University, Beijing 100875, People's Republic of China, and [§]Shanghai Key Laboratory of Magnetic Resonance, Physics Department, East China Normal University, Shanghai 200062, People's Republic of China

Visualization techniques constitute a powerful tool in defining microquantitative molecular events critical to biomedical research and clinical diagnostics.[1] In particular, a great deal of interest has been focused on visualization of the same target at different levels from the cellular scale to the whole body, because different molecular imaging methods, such as CT (computed tomography), magnetic resonance imaging (MRI), optical imaging, and nuclear medicine imaging, have different spatial resolutions, imaging depths, and areas of application.[2−6] A typical example is combining usage of CT and positron emission tomography (PET) to provide a clinical tool, PET/CT, for whole-body imaging. CT provides exceptional anatomical information, but suffers from limited sensitivity. PET provides a visualization method with high sensitivity (picomolar), albeit with a low (~mm) spatial resolution. Hence, the combination of PET/CT provides excellent spatial resolution and high sensitivity.[1−7] In addition, CT, PET, and MRI are all unsuitable for visualizing living cells because of low planar resolution, but this can be resolved by fluorescent bioimaging.

Photoluminescence imaging provides the highest spatial resolution (several hundreds of nanometers) and is suitable for imaging living cell,[8−10] but it lacks the full capability to obtain anatomical and physiological detail *in vivo* because of its limited penetration of light in tissue.[11] Ideally, to bridge gaps in sensitivity, resolution, and penetration depth of multilevel visualization from the cellular scale to whole-body animal, photoluminescence emission, radioactivity, and magnetic properties should be combined within one system for multilevel imaging. To date, some dual-modality bioimaging (especially optical/PET) have been developed;[12−20] however, few examples of multifunctional materials combining radioactivity, magnetic, and photoluminescence emission properties have been reported for trimodality bioimaging.[21,22]
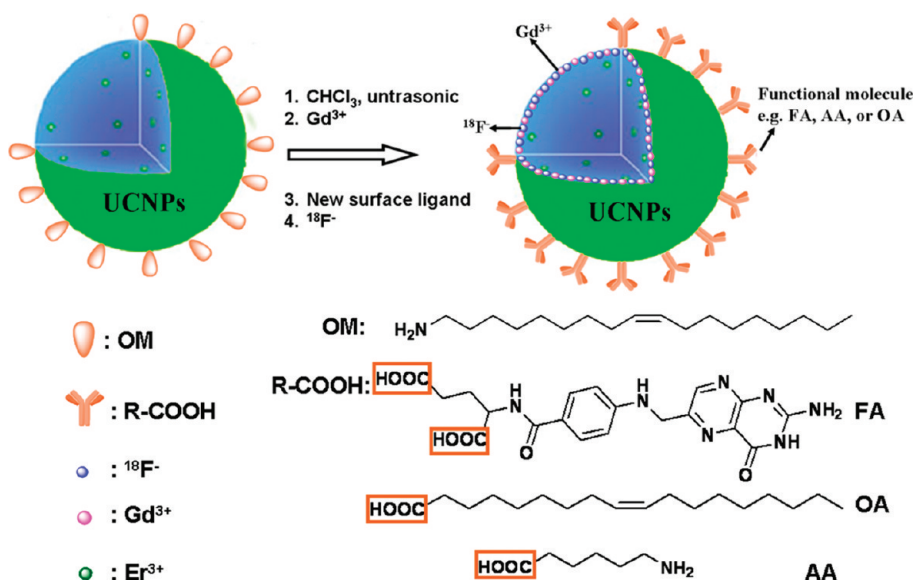
Due to their unique 4f electron structures, rare-earth ions display rich optical and magnetic properties, and rare-earth materials may be ideal building blocks for fabricating multifunctional bioprobes. The gadolinium ion (Gd^{3+}), having seven unpaired electrons, provides high paramagnetic relaxivity, and Gd^{3+}-containing materials are usually used as T_1-positive contrast agents.[23−25] Some nanoparticles co-doped with rare-earth ions show unique photoluminescent properties.[9,11,26−64] For example, under continuous-wave (CW) excitation at 980 nm, $NaYF_4$ nanoparticles doped with Yb^{3+} as a sensitizer and Er^{3+} (and/or Tm^{3+}, Ho^{3+}) as an activator display upconversion luminescence in the visible region. As a result, doping one system with different rare-earth ions becomes a powerful method for fabricating magnetic/optical difunctional materials. To date, several types of

ABSTRACT A novel method of rare-earth cation-assisted ligand assembly has been developed to provide upconversion nanophosphors with T_1-enhanced magnetic resonance (MR), radioactivity, and targeted recognition properties, making these nanoparticles potential candidates for multimodal bioimaging. The process of modifying the surface of the nanophosphors has been confirmed by transmission electron microscopy, X-ray powder diffraction, X-ray photoelectron spectroscopy, proton nuclear magnetic resonance, Fourier-transform infrared spectroscopy, energy-dispersive X-ray analysis, and so on. The versatility of this surface modification approach for incorporating functional molecules and fabricating fluorine-18-labeled magnetic-upconversion nanophosphors as multimodal bioprobes has been demonstrated by targeted cell imaging, *in vivo* upconversion luminescence, MR imaging, and positron emission tomography imaging of whole-body small animals.

KEYWORDS: upconversion nanophosphors · rare-earth cation · fluorine-18 · magnetic · multimodal

Scheme 1. Schematic of fluorine-18-labeled magnetic-upconversion functional nanocrystals. OM: oleyl amine; FA: folic acid; OA: oleic acid; AA: aminocaproic acid.

nanoparticles based on $NaYF_4$ or $NaGdF_4$ co-doped with Yb^{3+}, Er^{3+}/Tm^{3+}, and Gd^{3+} having upconversion luminescence (UCL) and magnetic resonance properties have been reported for T_1-positive MR and UCL *in vivo* dual-modality whole-body imaging of small animals.[18−20]

As an alternative to the method of doping with Gd^{3+} for MRI application, another strategy is surface modification of nanoparticles, because surface Gd^{3+} ions are mainly responsible for the T_1 enhancement in MRI. In the present article, we propose a novel and facile strategy (Scheme 1) for synthesizing multifunctional nanoparticles that integrate UCL ($NaYF_4$:Yb,Er), magnetism (Gd^{3+}), radioactivity (^{18}F), and targeted recognition (folic acid). Of particular note is that Gd^{3+} is not doped within the host materials, but is distributed on the surface of the nanocrystals by cation exchange with Y^{3+}. Hence, the nanocrystals possess novel magnetic resonance properties. The upconversion nanophosphors (UCNPs) modified by Gd^{3+} (Gd-UCNPs) can be further functionalized using a variety of capping molecules, imparting different surface functionalizations to the UCNPs depending on the molecules employed. ^{18}F has been introduced on the UCNPs through interaction with the rare-earth ions for PET imaging. Moreover, we have explored the cell-targeted imaging, and *in vivo* UCL, MR, and PET imaging of the obtained multifunctional UCNPs.

RESULTS AND DISCUSSION

Characterization of the Nanophosphors. The OM-UCNPs were synthesized according to a modified cothermolysis process.[46] They were soluble in nonpolar solvents (such as cyclohexane) owing to the presence of the organic ligand (OM) on the surface of the UCNPs. When a large volume of chloroform was added to a dispersion of the OM-UCNPs in cyclohexane, UCNPs were found to precipitate after 10 min of ultrasonication, revealing a remarkable change in solubility in nonpolar media due to cleavage of the OM from the surface of the UCNPs. Thus, UCNPs treated with chloroform under ultrasonication were no longer capable of dispersion in either nonpolar or polar solvents, necessitating their further modification. It is well known that the coordinating ability of the −COOH group toward rare-earth ions is quite strong. In the present study, oleic acid (OA), aminocaproic acid (AA), and folic acid (FA) were chosen as new functional ligands to functionalize the UCNPs. Before the assembly of these new ligands on the surface of the UCNPs, Gd^{3+} was introduced on the UCNPs by cation exchange, which not only imparted magnetic resonance properties but also increased the positive charge on the surface of the UCNPs, favoring the attachment of new carboxylic acid ligands. Radioactive $^{18}F^-$ for PET imaging could then be integrated on the UCNPs through interaction with the rare-earth ions, as shown in Scheme 1.

The morphology and structure of the UCNPs were characterized by transmission electron microscopy (TEM), dynamic light-scattering (DLS), and X-ray powder diffraction (XRD). The well-dispersed particles were coated with long-chain oleyl amine ligands, as shown in Figure 1a. Their sizes were in the range 10−20 nm, which is consistent with the DLS data (Figure S1a). After assembly of the carboxylic acid ligands (to form AA-Gd-UCNPs), the size of the water-dispersible nanoparticles increased to 22−30 nm (Figure 1b). DLS data (Figure S1b) revealed that the overall diameter of the UCNPs was increased by 6−14 nm, corroborating the assembly of the new carboxylic acid ligands. These facts indicated that the surface ligands were brushed off, depressing the surface passivation. HR-TEM (Figure 1c)
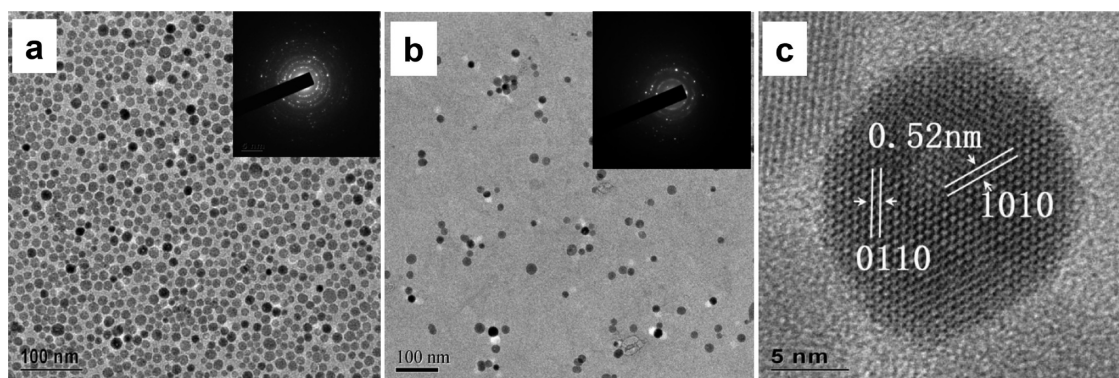
Figure 1. TEM of OM-UCNPs (a) and OA-Gd-UCNPs (b); (c) HR-TEM of OM-UCNPs. Inset in (a) and (b) is ED pattern of OM-UCNPs and AA-Gd-UCNPs, respectively.
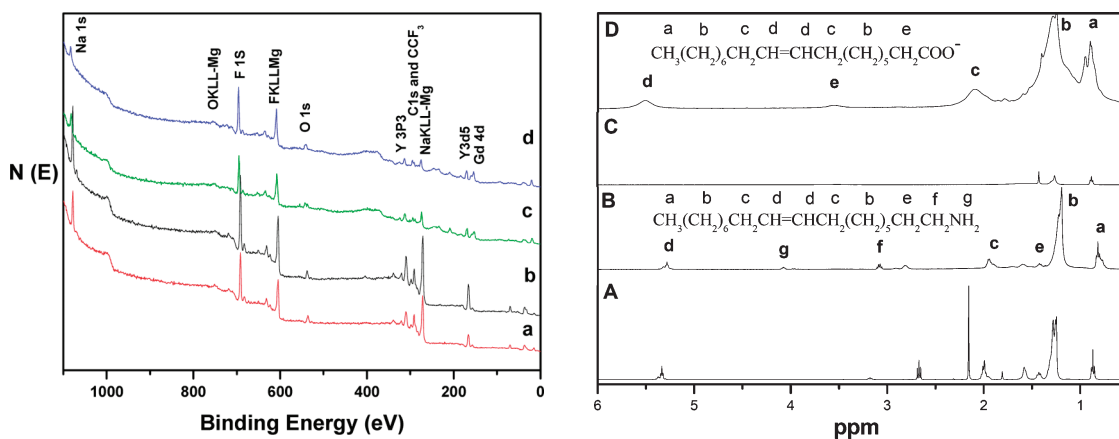

Figure 2. XPS of (a) OM-UCNPs, (b) UCNPs washed by cyclohexane and chloroform, (c) Gd-UCNPs, and (d) OA-Gd-UCNPs.

Figure 3. ^{1}HNMR of free OM (A), OM-UCNPs (B), Gd-UCNPs (C), and OA-Gd-UCNPs (D).

showed that the lattice distances were both 0.52 nm, corresponding to the (1010) and (0110) planes of a hexagonal phase, respectively. To further confirm the compositions and the crystallinities of the obtained OM-UCNPs and AA-Gd-UCNPs, the XRD patterns of the samples were studied (Figure S2). All of the positions and intensities of the diffraction peaks, both before and after ligand assembly, could be indexed to a pure hexagonal phase, in good agreement with the JCPDS data.

Characterization of Surface Modification. The surface modification involved two steps: first, Gd^{3+} was introduced on the UCNPs by cation exchange; then new ligands containing −COOH, which has a strong coordination ability toward rare-earth ions, were assembled. The cation exchange was monitored by XPS and EDXA. The full XPS spectrum is shown in Figure 2. Photoelectron spectra of Gd^{3+} $3d^5$ and $3d^3$ were recorded after its attachment. The Gd/Ln (Y, Yb, Gd) ratio was found to be about 1/2 by XPS analysis. Energy-dispersive X-ray analyses (EDXA) of both the OM-UCNPs and OA-Gd-UCNPs are shown in Figure S3. The EDXA patterns confirmed the presence of Na, Y, F, and Yb in the samples of both OM-UCNPs and OA-Gd-UCNPs, with

Gd appearing solely in the OA-Gd-UCNPs, and the Gd/Ln (Y, Yb, Gd) ratio was about 1/5. The difference in the Gd/Ln (Y, Yb, Gd) ratios estimated by XPS and EDXA may possibly be ascribed to the difference in detection depths, because XPS analyzes the surface elements of nanoparticles to a nanoscale depth, while EDXA analyzes the elements of the whole nanoparticles to a microscale depth.

In the present study, oleic acid and aminocaproic acid were chosen to assemble on the surface of the UCNPs as new ligands. The change of surface ligand on the UCNPs was tracked by ^{1}H NMR, FT-IR, TGA, amine content, and zeta-potential test. To avoid interference from the dopant ions (Yb^{3+}, Er^{3+}, and Tm^{3+}) on the ^{1}H NMR signal, undoped $NaYF_4$ nanoparticles were used in place of UCNPs for the ^{1}H NMR study. Figure 3 shows the ^{1}H NMR spectra of the moieties attached to the undoped $NaYF_4$ at the different stages of the ligand assembly process. The ^{1}H NMR spectrum of the as-prepared $NaYF_4$ sample dispersed in $CDCl_3$ (Figure 3B) exhibits the characteristic peaks of oleyl amine, which appear broadened compared with the spectrum of free oleyl amine in $CDCl_3$ (Figure 3A). Signal broadening of this type has been observed in a previous report on UCNPs.[51] After washing with chloroform under ultrasonication, no
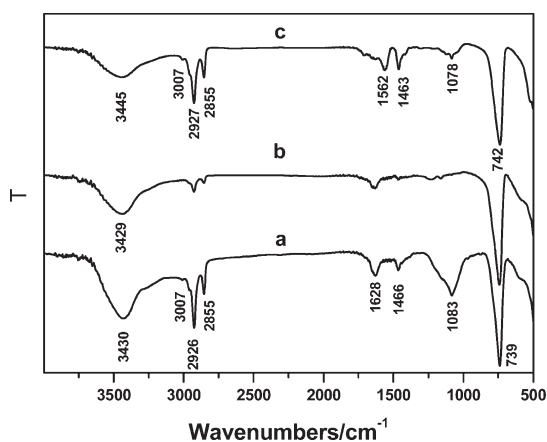
Figure 4. FT-IR spectra of (a) OM-UCNPs, (b) Gd-UCNPs, and (c) OA-Gd-UCNPs.

signal was detected in the spectrum shown in Figure 3C except that of a trace of impurity. After further treatment with the rare-earth cation and oleic acid, the ^1H NMR spectrum of $NaYF_4$ coated with oleic acid dispersed in $CDCl_3$ was also recorded (Figure 3D) and proved to be similar to the standard spectrum of oleic acid, apart from the broadening.

The successful accomplishment of ligand assembly was also verified by Fourier-transform infrared (FT-IR) analysis. In the course of preparation of the OM-UCNPs, oleyl amine was coated onto the outer face of the *in situ* generated UCNPs through the interaction between the rare-earth cation (Gd^{3+}) and the amino groups of the amine, with the hydrophobic alkyl chains directed toward the exterior. As a result, the OM-UCNPs were easily dispersed in a nonpolar solvent (such as hexane or chloroform). As shown in Figure 4a, transmission bands at 2926 and 2855 cm^{-1} attributable to asymmetric (ν_{as}) and symmetric (ν_s) stretching vibrations, respectively, of methylene (CH_2) in the long alkyl chains of OM were measured. Moreover, a peak at 3007 cm^{-1}, assigned to $=C-H$ stretching vibration, was clearly observed in the FT-IR spectrum of the OM-UCNP sample. However, this feature was apparently lost after washing with chloroform under ultrasonication (Figure 4b). Two bands at 1562 and 1463 cm^{-1}, corresponding to the in-plane bending vibration, and a restored characteristic band at 3007 cm^{-1} attributable to $=C-H$ stretching vibration were observed for the oleic acid-coated nanoparticles (Figure 4c).

To evaluate the amount of ligand on both the as-prepared and chloroform-washed UCNP samples, thermogravimetric analysis (TGA) was performed (Figure S4). It is clear that the amount of oleyl amine ligands on the present as-prepared samples was about 18.4 wt %; however, only 5.6 wt % of this ligand remained on the surface after washing with chloroform under ultrasonication, suggesting that the bulk of the ligand was removed during the washing. The remainder may possibly be attributed to the presence of CF_3COO^-,
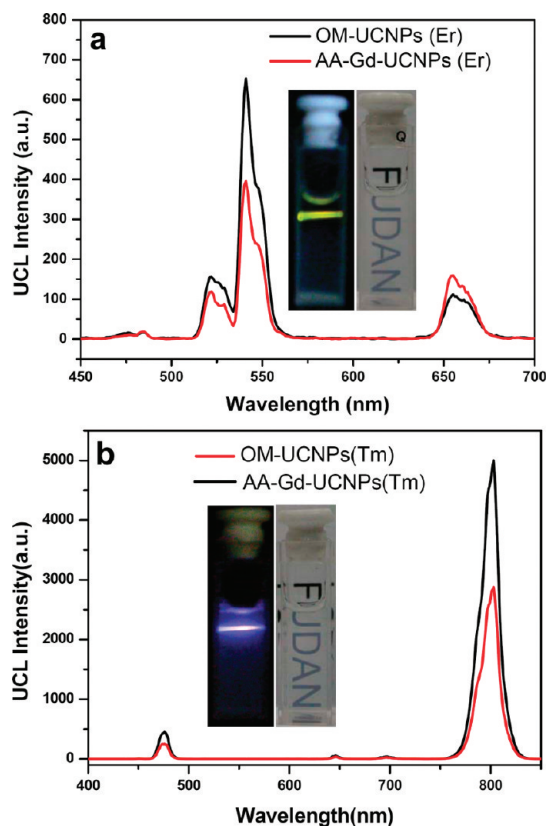

Figure 5. Room-temperature upconversion luminescence spectra of OM-UCNPs (1 mg/mL) in cyclohexane and AA-Gd-UCNPs (1 mg/mL) in water. The inset shows luminescence and bright-field photos of 1 mg/mL AA-Gd-UCNPs (Er) (a) and 1 mg/mL AA-Gd-UCNPs (Tm) (b) in water under CW excitation at 980 nm (power ≈ 1000 mW).

which did not decompose completely and was en-wrapped in the nanoparticles in the process of fast nucleation, as indicated by XPS data (Figure S5).

When the ligand was changed to aminocaproic acid, the amount of amine could be determined by means of Fmoc protection and a standard Fmoc quantification protocol. The amine content of the UCNPs was determined to be $(5.6 \pm 0.8) \times 10^{-5}$ mol/g (Figure S6). The effects of the ligand-exchange process were further investigated on the basis of the zeta-potential. The zeta-potential of the OM-UCNPs was estimated as about +12 mV in ethanol. Upon treatment with Gd^{3+}, it changed to a more positive +25 mV, which confirmed that Gd^{3+} had been introduced on the surface of the UCNPs. When the new ligands had been assembled, the zeta-potential decreased to +18 mV, which resulted from coordination between the exterior cations and the new ligands.

On the basis of the above-described ^1H NMR, FT-IR, TGA, amine content, and zeta-potential results, it can be deduced that the oleyl amine ligand was removed by washing with chloroform under ultrasonication and that the new carboxylic acid ligands (oleic acid or aminocaproic acid) were assembled on the surface of UCNPs by adding them in conjunction with Gd^{3+}.
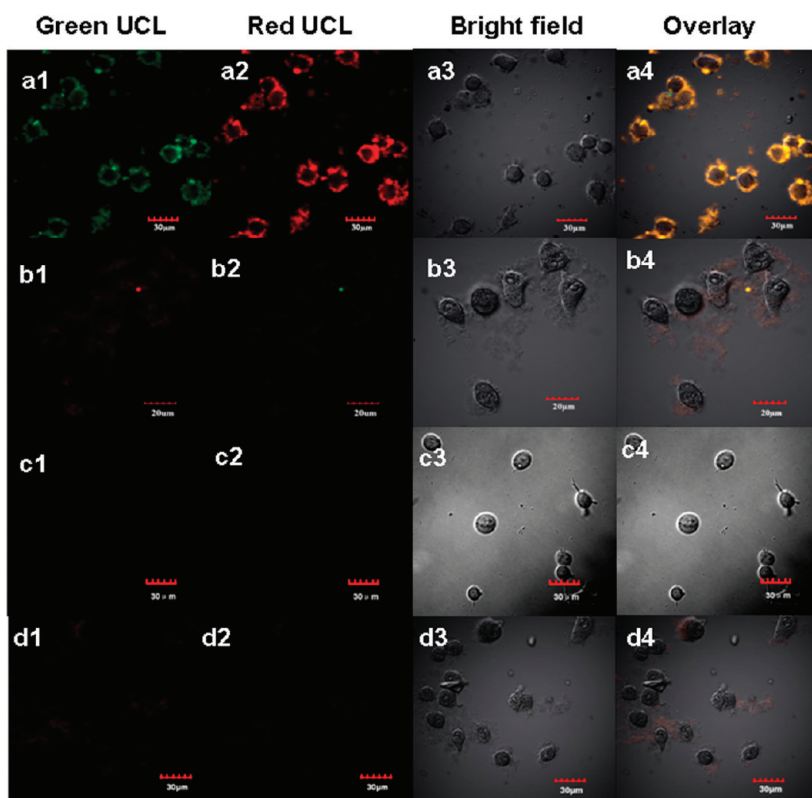
Figure 6. Confocal luminescence imagings of FR(+) KB (a) and FR(−) MCF-7 cells (c) stained with 200 μg mL^{-1} FA-AA-Gd-UCNPs nanocomposites for 1 h at 37 °C (λ = 980 nm). Part b shows the materials comparison experiments of FR(+) KB cells incubated with AA-Gd-UCNPs under the same conditions, while the competitive experiments with FA is shown in part d. (1) λ_{em} = 520−560 nm and (2) λ_{em} = 640−680 nm, bright-field image of cells shown in panel 3. (4) Overlay image of 1, 2, and 3.

Upconversion Luminescence. No obvious change in the UCL wavelength and sharpness except a slight decrease in luminescence intensity was observed before and after assembly of the new ligands, which may be attributed to the change of ligands and solvent. Figure 5a shows the room-temperature UCL spectra of OM-UCNPs and AA-Gd-UCNPs doped with Er^{3+} in the wavelength region 500−700 nm. Bright-green emissions at 521 and 540 nm, corresponding to the $^4H_{11/2} \rightarrow {}^4I_{15/2}$ and $^4S_{3/2} \rightarrow {}^4I_{15/2}$ transitions, and a weak red emission at 654 nm, attributable to the $^4F_{9/2} \rightarrow {}^4I_{15/2}$ transition, were observed in cyclohexane and water, respectively. Figure 5b shows the UCL spectrum of Tm^{3+}-doped UCNPs under CW excitation at 980 nm. The upconversion luminescence emission at around 475 nm is originated from the transition $^1G_4 \rightarrow {}^3H_6$, and emission at 800 nm can be attributed to the transition $^3H_4 \rightarrow {}^3H_6$, which is an ideal wavelength for *in vivo* imaging because of the deeper tissue penetration. Corresponding upconversion luminescence images of the AA-Gd-UCNPs are shown in the insets of Figure 5a and b, respectively. For further application in bioimaging, the stability of AA-Gd-UCNPs suspension dispersed in PBS was determined by UCL spectra. As shown in Figure S7, even though 48 h later, the UCL intensity of AA-Gd-UCNPs dispersed in PBS is mostly the same as those of the original state (0 h in PBS) and

in water. The inset of Figure S7 shows the bright-field photo of AA-Gd-UCNPs dispersed in PBS for 0 and 48 h.

Cytotoxicity and Cell Imaging. To ascertain whether FA had been capped on the surface of the UCNPs, cellular targeted imaging was required. However, before commencing such targeted imaging experiment, it was necessary to investigate the cytotoxicity of the FA-AA-Gd-UCNPs. The cytotoxicity of UCNPs doped with Er^{3+}, which were designed to be used as a probe for cell imaging, was tested. On the basis of the reduction activity of methyl thiazolyl tetrazolium (MTT), increasing concentrations of the nanoparticles were incubated with KB cells and cell viability was assessed. The viability of the untreated cells was assumed to be 100%. The results are shown in Figure S8. The cell viability was higher than 95% for all doses, even after 10 h of exposure. These data show that FA-AA-Gd-UCNPs can be considered to have low cytotoxicity.

To determine whether UCNPs coated with folic acid and aminocaproic acid (FA-AA-Gd-UCNPs, FA:AA = 1:9) could be used for cellular targeted imaging, we performed *in vitro* cellular studies using FR-positive [FR(+)] KB cell lines and FR-negative [FR(−)] MCF-7 cell lines. The ability of FA-AA-Gd-UCNPs to target FR(+) cells was evaluated by means of a laser scanning upconversion luminescence microscope (LSUCLM) equipped with CW excitation at 980 nm.[7] Under CW excitation at 980 nm,

Bright field **UCL** **Overlay**

In vivo

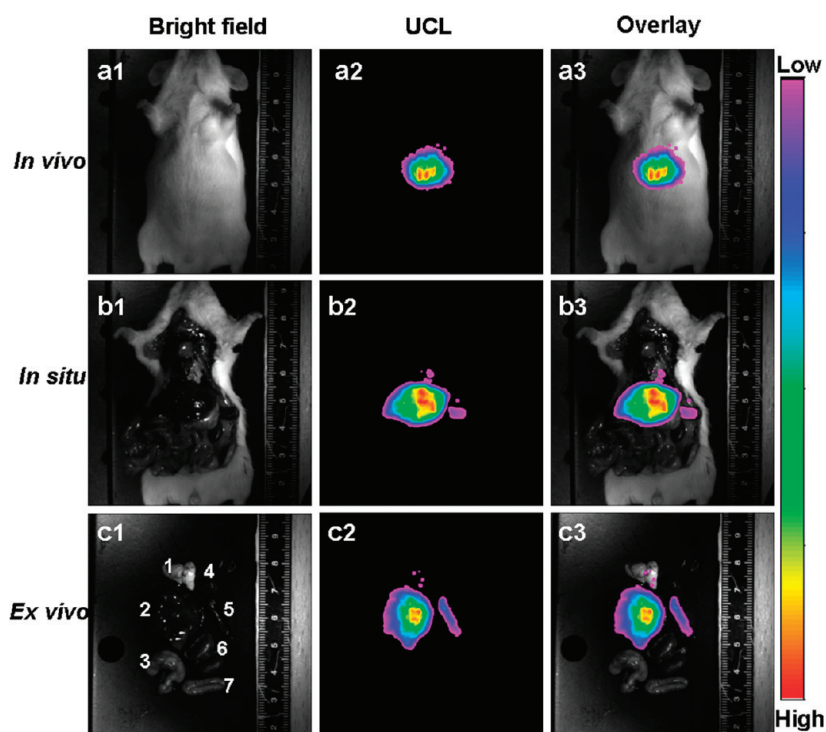*In situ*

Ex vivo

Low

High

Figure 7. *In vivo* (a), *in situ* (b), and *in vitro* (c) upconversion imaging at 10 min postinjection of AA-Gd-UCNPs. 1, lung; 2, liver; 3, stomach; 4, heart; 5, spleen; 6, kidney; 7, intestines.

a strong luminescence signal was observed from the KB cells after 1 h of incubation at 37 °C (Figure 6a1, a2), while the MCF-7 cells showed much lower luminescence (Figure 6c1, c2). Moreover, the luminescence intensity obtained from the live KB cells was much higher than that obtained from the MCF-7 cells. Additionally, overlays of confocal luminescence (Figure 6a4) and bright-field images (Figure 6a3) demonstrated that the luminescence was evident on the surface of the KB cells. Furthermore, confocal luminescence imaging data collected as a series along the *Z*-optical axis (*Z*-stack) (Figures S9 and S10) verified that the luminescence signal of the nanocomposites was indeed localized on the KB cells. These results imply that the KB cells express a higher amount of folate receptor than the MCF-7 cells and that the FA-AA-Gd-UCNPs selectively accumulate on the surface of the FR(+) KB cells. To support the receptor-mediated endocytosis of the nanocomposites, we also conducted competition experiments and material comparison experiments under the same experimental conditions. The competition experiments were conducted by simultaneously incubating FR(+) KB cells with excess free FA or FA-AA-Gd-UCNP nanocomposites at 37 °C for 1 h. As a result, only weak luminescence was observed, as shown in Figure 6d (bottom panel). The competing nanocomposite used in the material comparison experiments was AA-Gd-UCNPs, with which very weak signals were detected, as shown in Figure 6b. All of the above results suggested that FA had indeed been capped on the surface of UCNPs by

the surface-modification process and that the folate receptor-mediated targeted delivery was effective.

In Vivo Upconversion Imaging. To demonstrate the capability of AA-Gd-UCNPs doped with Tm^{3+} to serve as a nanoprobe for optical bioimaging, we performed *in vivo* upconversion luminescence imaging of Kunming mice through tail vein injection of these nanoparticles (200 μL, 0.5 mg/mL per animal). Analyses of Figure 7a revealed that nanoparticle aggregates were distributed in the liver and spleen. Rapid accumulation in the liver and spleen and relatively slow excretion are classical behaviors of *in vivo* nanoparticles, since the liver contains phagocytic cells and the liver and spleen are the main organs for eliminating foreign particles. As is well known, nanoparticle aggregation in living animals can lead to significant uptake in the lungs, so the observation of quite weak upconversion signal from the lungs in *in situ* (Figure 7b) and *ex vivo* (Figure 7c) studies suggests no significant aggregation of the AA-Gd-UCNPs in the above-mentioned experiments. Notably, although the upconversion nanomaterials improve the penetration greatly as optical imaging probe, to date, it still lacks the full capability to obtain anatomical and physiological detail *in vivo*.

Relaxivity Measurement and in Vivo MRI. MRI can provide an excellent spatial resolution and depth for *in vivo* imaging and can provide exceptional anatomical information. Gadolinium (Gd^{3+}), as a member of the rare-earth ions, has been used in MRI as a positive contrast agent. Owing to the presence of Gd^{3+} on the surface of AA-Gd-UCNPs, these particles could also act as a T_1 MRI
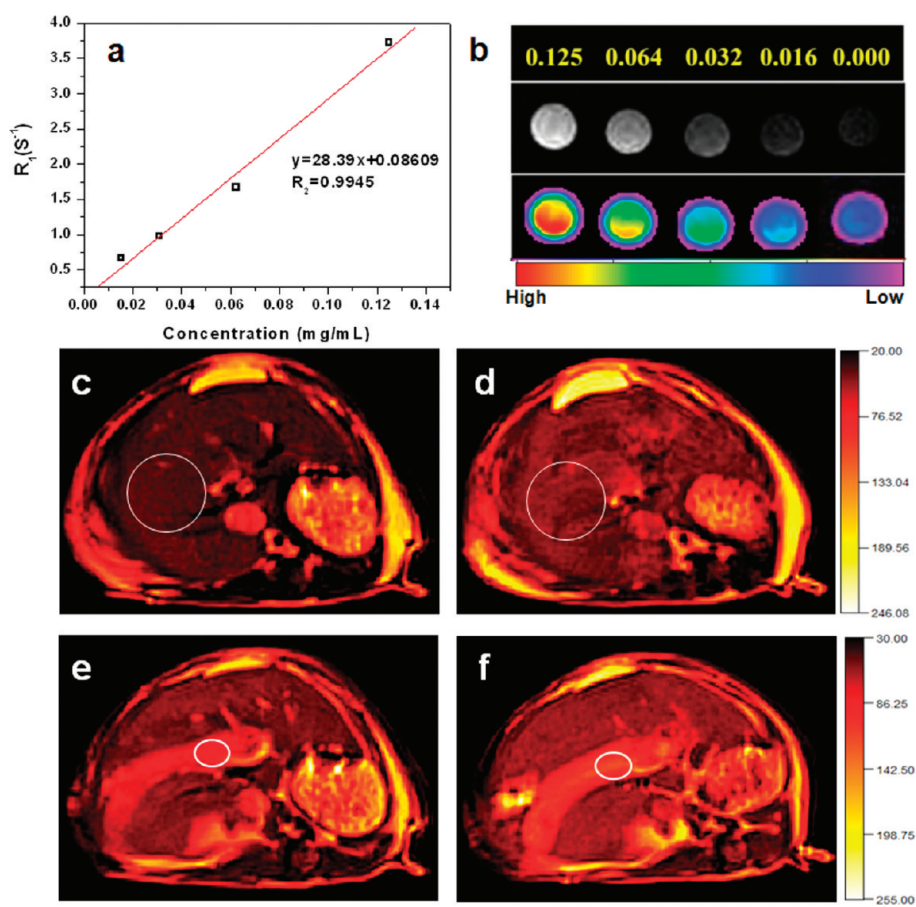
Figure 8. (a) Relaxation rate R_1 ($1/T_1$) *versus* various mass concentration (0.125, 0.064, 0.032, 0.016 mg/mL) of AA-Gd-UCNPs at room temperature using a 3 T MRI scanner. (b) T_1-weight and color-mapped MR images of various concentrations (0.125, 0.064, 0.032, 0.016 mg/mL) of AA-Gd-UCNPs. Deionized water (0 mg/mL) was the reference. Magnetic resonance images of transversal cross-sectional images of the liver (c, d) and spleen (e, f) of mouse at preinjection and at 10 min postinjection of the AA-Gd-UCNPs.

contrast agent. Figure 8a displays the T_1-weighted relaxivity in the range 0.016–0.125 mg/mL, which shows a signal that was enhanced by increasing AA-Gd-UCNP concentrations. A good linear relationship was observed when the mass concentration of the AA-Gd-UCNPs was plotted against R_1. The relaxivity parameter (r_1) calculated from the slope of the concentration-dependent relaxation $1/T_1$ (R_1) is also shown in Figure 8a. Based on the slope, the value of r_1 at 38 °C and 3 T magnetic strength was estimated to be 28.39 s^{-1} $(mg/mL)^{-1}$. Although a precise explanation for the good relaxation properties requires further research, the enhancement of r_1 can be explained by considering the increased amount of Gd on the surface of the UCNPs. In addition, Figure 8b displays T_1-weighted and color-mapped images in the range 0–0.125 mg/mL. This study has demonstrated that the Gd^{3+}-containing UCNPs could indeed serve as an effective T_1 MRI contrast agent. Furthermore, relaxivity measurement *in vitro* of AA-Gd-UCNPs incubated in PBS for 48 h (Figure S11) was also performed. After incubating in PBS, the relaxivity of AA-Gd-UCNPs is around the value in water (28.39 S^{-1}).

Moreover, the feasibility of using AA-Gd-UCNPs as a contrast agent for MRI *in vivo* was tested. To evaluate the positive contrast enhancement of AA-Gd-UCNPs *in vivo*, anatomical images were acquired in the transversal planes. Comparison of pre- and postcontrast T_1-weighted transversal cross-sectional images of mice revealed significant contrast enhancement in the liver area (region 1 in Figure 8c, d) and spleen area (region 2 in Figure 8e,f), which further confirmed the accumulation of the nanomaterials in these organs. At 10 min postinjection of AA-Gd-UCNPs, the enhancements in signal intensities in the liver and spleen were determined as 29.4% and 30.5%, respectively. These results verified that AA-Gd-UCNPs could be applied as an MRI positive-contrast agent.

***In Vivo* PET Imaging.** MRI is capable of providing precise anatomical information, yet suffers from low signal sensitivity; so integrating MRI and PET is required for *in vivo* imaging. Radio-TLC analysis demonstrated a 92% labeling yield of ^{18}F-AA-Gd-UCNPs. Even after 2 h incubation in PBS, the ^{18}F-labeling yield is still more than 90%. *In vivo* PET imaging was performed in a Siemens Inveon small-animal micro-PET scanner,
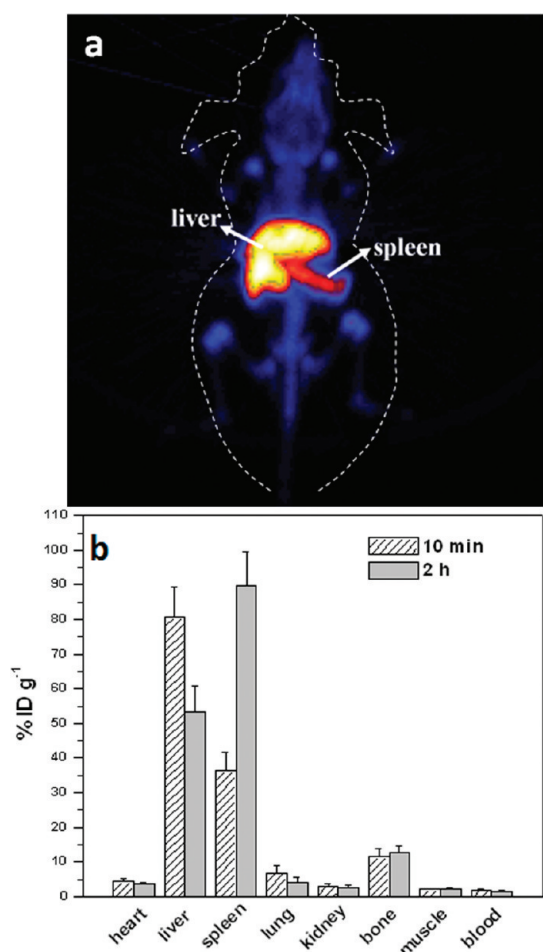
Figure 9. (a) Kunming mice PET imaging 10 min postinjection of ^{18}F-AA-Gd-UCNPs (200 μg/mL). (b) Biodistribution of ^{18}F-AA-Gd-UCNPs at 10 min and 2 h postinjection; the data shown are based on five mice per group.

whereby an image was acquired at 10 min postinjection, as shown in Figure 9a. Intense radioactivity signals were observed exclusively in the liver and spleen, which confirmed that ^{18}F-AA-Gd-UCNPs had been rapidly taken up by these two organs. The results were consistent with those from UCL imaging and MRI. Moreover, considering that free ^{18}F^{-} has an innate bone-targeting ability, the low radioactivity signal from bone indicated that most of the ^{18}F radiolabel was

retained on the ^{18}F-AA-Gd-UCNPs in the course of the experiment. The result was further confirmed by *ex vivo* biodistribution. As shown in Figure 9b, rapid accumulation of nanoparticles was found in the liver [~80.8% of the injected dose (ID)/g] and spleen (~36.6% ID/g) at 10 min, while at 2 h the liver uptake decreased to ~53.5% ID/g, and the spleen accumulation increased to 89.9% ID/g. Uptake in the heart, lungs, kidney, and other organs (including bone) was very low (<13% ID/g). In addition, these features attested that the ^{18}F-labeling and *in vivo* PET imaging strategy described here provides a facile method for real-time tracking with high sensitivity for bioimaging *in vivo*.

CONCLUSION

In conclusion, a novel strategy for modifying the surface of upconversion nanophosphors has been developed, which imparts them with excellent upconversion luminescence properties, MR, radioactivity, targeted function, and water- and biocompatibility, thereby making these nanoparticles a potential candidate for multimodal bioimaging. The versatility of this surface modification approach for incorporating functional molecules and fabricating radioactive magnetic-upconversion nanophosphors has been demonstrated by means of cellular targeted imaging, MRI, *in vivo* upconversion luminescence imaging, and PET imaging, and the as-synthesized UCNPs obtained by rare-earth cation-assisted ligand assembly can indeed be applied as a trimodal probe. In particular, the strategy of introducing Gd^{3+} by cation exchange supersedes previous methods of Gd^{3+}-doping or using a host material containing Gd^{3+}, since surface Gd^{3+} ions are mainly responsible for the T_1 enhancement in MRI, and the value of r_1 is 28.39 s^{-1} (mg/mL)$^{-1}$. This study opens up new perspectives for the preparation of uniform nanoprobes for multimodal bioimaging application from the cellular scale to whole-body evaluation. Furthermore, this strategy may provide great potential for designing further multifunctionalized upconversion nanophosphors owing to the possibility of varying the rare-earth ion and the new ligand.

MATERIALS AND METHODS

Materials. All starting materials were obtained from commercial supplies and used as received. Rare earth oxides Y$_2$O$_3$ (99.999%), Yb$_2$O$_3$ (99.999%), Er$_2$O$_3$ (99.999%), Tm$_2$O$_3$ (99.999%), and Gd$_2$O$_3$ (99.999%), were purchased from Shanghai Yuelong New Materials Co. Ltd. Oleyl amine (OM) (>90%) and oleic acid (OA) were purchased from Alfa Aesar Ltd. Aminocaproic acid (AA), folic acid (FA), hydrochloric acid, and trifluoroacetic acid (99%) were supplied from Sinopharm Chemical Reagent Co., Ltd. (Shanghai). All other chemical reagents of analytical grade were used directly without further purification. Deionized water was used throughout. RE(CF$_3$COO)$_3$ were prepared with the

literature method.[65] GdCl$_3$ was prepared by dissolving the Gd$_2$O$_3$ and hydrochloric acid at elevated temperature.

Characterization. Powder X-ray diffraction measurements were performed on a Bruker D4 diffractometer at a scanning rate of 1 °C/min in the 2θ range from 10° to 70° (Cu Kα radiation, λ = 1.54056 Å). The size and morphology of UCNPs were determined at 200 kV at a JEOL JEM-2010 low- to high-resolution transmission electron microscope (HR-TEM). These as-prepared samples were dispersed in cyclohexane and dropped on the surface of a copper grid for TEM testing. ^{1}H NMR spectra were recorded on a Varian Mercury 400 spectrometer. Proton chemical shifts are reported in parts per million downfield from

tetramethylsilane. Fourier transform infrared spectra were performed using an IRPRESTIGE-21 spectroscope (Shimadzu) with KBr pellets. The wavenumber range recorded was 400−4000 cm^{-1}. Thermogravimetric analysis curves were recorded on a DTG-60H (Shimadzu) at a heating rate of 10 °C/min. The upconversion luminescence emission spectra were recorded on an Edinburgh LFS-920 instrument, but the excitation source was an external 0−2 W adjustable 980 nm semiconductor laser (Beijing Hi-Tech Optoelectronic Co., China) with an optic fiber accessory, instead of the Xeon source in the spectrophotometer. The images of upconversion luminescence were obtained digitally on a Nikon multiple CCD camera. Dynamic light scattering and zeta-potential experiments were carried out on an ALV-5000 spectrometer-goniometer equipped with an ALV/LSE-5004 light scattering electronic and multiple tau digital correlator and a JDS Uniphase He−Ne laser (632.8 nm) with an output power of 22 mW. The size distribution was measured at 25 °C with a detection angle of 90°. XPS experiments were carried out on a RBD upgraded PHI-5000C ESCA system (Perkin-Elmer) with Mg Kα radiation ($h\nu$ = 1253.6 eV) or Al Kα radiation ($h\nu$ = 1486.6 eV).

Synthesis of Oleyl Amine Capped UCNPs [abbreviated as OM-UCNPs]. Various UCNPs without ligands at the surface were prepared by a modified co-thermolysis process.[44] A 4 mmol amount of CF_3COONa and 2 mmol (total amounts) of $Ln(CF_3COO)_3$ (Ln: 78 mol %Y + 20 mol % Yb + 2 mol % Er/1 mol % Tm) were added to 20 mL of OM in a 100 mL three-neck round-bottom flask at room temperature. Next, the reaction solution was directly heated to 120 °C to remove water and oxygen, with vigorous magnetic stirring in the current of argon for 1 h. At this point, the reaction mixture was a transparent solution. Then the solution was heated to 320 °C under argon at a rate of 10 °C per minute and maintained at this temperature for 1 h. After the reaction was complete, 10 mL of cyclohexane was poured into the solution at room temperature. The resultant mixture was centrifugally separated (15455g, 8 min every time in 20 °C), and the products were collected, named OM-UCNPs. The centrifugal separation was carried out by a Sigma 3K30 centrifugal machine. The as-precipitated nanocrystals were washed with cyclohexane and chloroform three times and dried under vacuum at room temperature overnight.

Synthesis of Gd^{3+}-Capped UCNPs [abbreviated as Gd-UCNPs]. The as-prepared OM-UCNPs were washed with cyclohexane and chloroform three times and dried under vacuum at room temperature overnight. Aqueous $GdCl_3$ solution (0.5 mM, 5 mL) was added to UCNPs (50 mg) in a 10-mL round-bottomed flask. Initially, all of the UCNPs remained at the bottom of the round-bottomed flask. The mixture was then stirred to transparency at room temperature, within several minutes, such that the UCNPs were homogeneously dispersed in the aqueous solution. After centrifugation (15455g, 8 min every time in 20 °C) and repeated washing of the collected solid with water, the precipitate was redispersed in deionized water until further utilization.

Assembly of Carboxylic Ligand [abbreviated as AA/OA/FA-Gd-UCNPs, FA-AA-Gd-UCNPs]. Aqueous solutions of aminocaproic acid/oleic acid/folic acid (2 mmol in total) or of aminocaproic acid (1.8 mmol) and folic acid (0.2 mmol) were added to Gd-UCNPs (50 mg) in a 10 mL round-bottomed flask. Initially, the nanoparticles were dispersed in the water by ultrasonication, and then the mixture was stirred for 1 h at room temperature to obtain a homogeneous phase. Thereafter, the mixture was centrifuged (15455g, 8 min every time in 20 °C), and the collected solid was repeatedly washed with water. The precipitate could be redispersed in deionized water or other polar solvents. UCNPs modified by AA/OA/FA or AA and FA were designated as AA/OA/FA-Gd-UCNPs and FA-AA-Gd-UCNPs, respectively.

Synthesis of ^{18}F-Labeled AA-Gd-UCNPs [abbreviated as ^{18}F-AA-Gd-UCNPs]. The as-prepared AA-Gd-UCNPs (0.2 mg) were mixed with 0.4 mL of aqueous solution of [18]F^- (~170 MBq) at room temperature, and the mixture was then treated by sonication for 10 min. ^{18}F-AA-Gd-UCNPs was obtained by centrifugation (15455g, 8 min every time in 20 °C). The ^{18}F-AA-Gd-UCNPs were washed three times with distilled water by sonication and

centrifugation.[66,67] Radio-TLC analysis showed that the labeling yield of ^{18}F-AA-Gd-UCNPs was 92%.

Cell Culture. A human nasopharyngeal epidermal carcinoma cell line (KB cell) was provided by the Institute of Biochemistry and Cell Biology, SIBS, CAS (China). Cells were grown in RPMI 1640 (Roswell Park Memorial Institute's medium) supplemented with 10% FBS (fetal bovine serum) at 37 °C and 5% CO_2. Cells (5×10^8/L) were plated on 14 mm glass coverslips under 100% humidity condition and allowed to adhere for 24 h.

Cytotoxicity of FA-AA-Gd-UCNPs. *In vitro* cytotoxicity was measured by performing MTT assays on the KB cells. Cells were seeded onto a 96-well cell culture plate at 5×10^4/well, under 100% humidity, and were cultured at 37 °C and 5% CO_2 for 24 h; different concentrations of FA-AA-Gd-UCNPs (0, 200, 400, and 800 μg/mL, diluted in RPMI 1640) were then added to the wells. The cells were subsequently incubated for 10 h at 37 °C under 5% CO_2. Thereafter, MTT (10 μL; 5 mg/mL) was added to each well, and the plate was incubated for an additional 4 h at 37 °C under 5% CO_2. After the addition of 100 μL of DMSO, the assay plate was allowed to stand at room temperature for 2 h. The OD570 value (Abs) of each well, with background subtraction at 690 nm, was measured by means of a Tecan Infinite M200 monochromator-based multifunction microplate reader. The following formula was used to calculate the inhibition of cell growth: Cell viability (%) = (mean of Abs value of treatment group/mean Abs. value of control) × 100%.

Cellular Staining. To ensure complete dispersion of the FA-AA-Gd-UCNPs in the serum-free media, their solutions (200 μg/mL) obtained from a stock suspension were sonicated for 30 min. For single-label imaging, KB cells were stained with 100 μg/mL FA-AA-Gd-UCNPs in a 5% CO_2 incubator at 37 °C for 1 h. Living cell imaging was then carried out after washing the cells with PBS three times to remove the excess FA-AA-Gd-UCNPs.

Confocal Imaging of FA-AA-Gd-UCNPs Incubated Living Cells. Confocal imaging of cells was performed with a modified Olympus FV1000 laser scanning confocal microscope equipped a continuous-wave NIR laser operating at 980 nm (Connet Fiber Optics, China).[7] A 60× oil-immersion objective lens was used. For the FA-AA-Gd-UCNPs, the CW NIR laser operating at 980 nm provided the excitation, and emission was collected at 540 ± 20 and 660 ± 20 nm.

In Vivo Upconversion Imaging. Kunming mice (~20 g) were anesthetized (with 10% chloral hydrate, 100 μL) and were injected intravenously with the AA-Gd-UCNPs solution (200 μL, 0.5 mg/mL). Ten minutes later, the upconversion imaging was performed utilizing the upconversion imaging equipment developed by our group[9] and a power density of 150 mW/cm^2.

Relaxivity Measurement *in Vitro*. The T_1-weighted MR images were obtained using a 3 T Siemens Magnetom Trio running on Siemens' Syngo software version B15 (Siemens Medical Systems), in conjunction with an 8 array loop coil (Siemens Medical Systems). Dilutions of AA-Gd-UCNPs (0.125, 0.064, 0.032, 0.016 mg/mL) in deionized water were placed in a series of 1.5 mL tubes for T_1-weighted MR imaging and T_1-weighted contrast enhancement. The following parameters were adopted: a standard inversion recovery (IR) spin−echo sequence: a repetition time (TR) of 6500 ms, an echo time (TE) of 7.6 ms, and 10 inversion recovery times (TI = 23, 100, 200, 400, 600, 800, 1000, 1200, 1500, 2000, and 3000 ms). Flip angle = 120°, slice thickness = 3.0 mm, FOV read = 190 mm, base resolution = 320. The MR signal intensity in the tubes was ascertained by the average intensity in the defined regions of interests. T_1 values of each tube were calculated using the following formula: $S(TI) = S_0 \times [1 - 2\exp(-TI/T_1)]$ to fit the T_1 recovery curve in the circular regions of interest for the sample. The resulting T_1 values were averaged over the region of interest and plotted as $1/T_1$ (R_1) *vs* molar concentration of AA-Gd-UCNPs. The slope of the line provides the molar relaxivity, r_1.

Magnetic Resonance Imaging in Vivo. Animal procedures were in agreement with the guidelines of the Regional Ethics Committee for Animal Experiments. *In vivo* experiments were performed on anesthetized mice (~20 g) with 10% chloral hydrate, 100 μL. MRI was conducted on a 3 T Siemens Magnetom Trio, using a T_1-mapping sequence (TR = 150 ms,

TE = 13 ms, flip angle = 5° and 18.596°, voxel size = 0.3 × 0.3 × 2 mm, slice thickness = 2.0 mm, FOV read = 80 mm). The mice were scanned before and after the administration of contrast agent. The PBS solution (150 μL) of the hydrophilic AA-Gd-UCNPs (0.2 mg/mL) was injected intravenously, and MRI transversal cross section images were obtained for each animal, which maintained normal body temperature for over 30 min.

***In Vivo* Positron Emission Tomography Imaging and *ex Vivo* Biodistribution.** For PET imaging, ^{18}F-AA-Gd-UCNPs ($\sim$6.0 MBq, 30 μg) in 100 μL of saline were injected into an anesthetized mouse ($\sim$20 g in body weight) through the tail vein under authorization of the Regional Ethics Committee for Animal Experiments. PET images were recorded on a Siemens Inveon small-animal PET scanner, with a typical acquisition time of 10 min. For biodistribution studies, ^{18}F-AA-Gd-UCNPs ($\sim$151 kBq) in 100 μL of saline were injected into mice. The major organs were collected and weighed at 10 min and 2 h postinjection. Radioactivity in the organs was measured using a γ-counter (WIZARD 1470, PerkinElmer Wallac, USA) and calibrated against a known aliquot of the injectate. Values are presented as mean ± standard deviation for five animals per group.

Supporting Information Available: (1) Hydrodynamic diameter distribution (from DLS) of OM-UCNPs and AA-Gd-UCNPs, (2) XRD of OM-UCNPs and AA-Gd-UCNPs, (3) EDXA of OM-UCNPs and AA-Gd-UCNPs, (4) TGA of freshly prepared OM-UCNPs and prepared UCNPs washed with cyclohexane and chloroform, (5) XPS of carbon of OM-UCNPs, Gd-UCNPs, and AA-Gd-UCNPs, (6) quantitative analysis of amine moieties of AA-Gd-UCNPs, (7) stability of the prepared multimodal probe in PBS by UCL spectra, (8) cytotoxicity data for FA-AA-Gd-UCNPs at different concentrations, (9) Z-stack confocal imaging of live KB cells, (10) three-dimensional luminescence images of live KB cells, (11) stability of the prepared multimodal probe in PBS by relaxation rate, (12) ^{18}F labeling yields of AA-Gd-UCNPs incubated in PBS for 10 min and 2 h. This material is available free of charge *via* the Internet at http://pubs.acs.org.

REFERENCES AND NOTES

1. Bogdanov, A. A., Jr. In *Molecular Imaging: An Essential Tool in Preclinical Research, Diagnostic Imaging, and Therapy*; Licha, K., Ed.; Springer: Berlin, 2004.
2. Cheon, J.; Lee, J. H. Synergistically Integrated Nanoparticles as Multimodal Probes for Nanobiotechnology. *Acc. Chem. Res.* **2008,** *41*, 1630–1640.
3. Kim, J.; Piao, Y.; Hyeon, T. Multifunctional Nanostructured Materials for Multimodal Imaging, and Simultaneous Imaging and Therapy. *Chem. Soc. Rev.* **2009,** *38*, 372–390.
4. Ametamey, S. M.; Honer, M.; Schubiger, P. A. Molecular Imaging with PET. *Chem. Rev.* **2008,** *108*, 1501–1516.
5. Patel, D.; Kell, A.; Simard, B.; Xiang, B.; Lin, H. Y.; Tian, G. H. The Cell Labeling Efficacy, Cytotoxicity and Relaxivity of Copper-Activated MRI/PET Imaging Contrast Agents. *Biomaterials* **2011,** *32*, 1167–1176.
6. van Schooneveld, M. M.; Cormode, D. P.; Koole, R.; van Wijngaarden, J. T.; Calcagno, C.; Skajaa, T.; Hilhorst, J.; 't Hart, D. C.; Fayad, Z. A.; Mulder, W. J. M.;*et al.*A Fluorescent, Paramagnetic and PEGylated Gold/Silica Nanoparticle for MRI, CT and Fluorescence Imaging. *Contrast Media Mol. I* **2010,** *5*, 231–236.
7. Pimlott, S. L.; Sutherland, A. Molecular Tracers for The PET and SPECT Imaging of Disease. *Chem. Soc. Rev.* **2011,** *40*, 149–162.
8. Conchello, J. A.; Lichtman, J. W. Optical Sectioning Microscopy. *Nat. Methods* **2005,** *2*, 920–931.
9. Yu, M.; Li, F.; Chen, Z.; Hu, H.; Zhan, C.; Yang, H.; Huang, C. Laser Scanning Up-conversion Luminescence Microscopy for Imaging Cells Labeled with Rare-Earth Nanophosphors. *Anal. Chem.* **2009,** *81*, 930–935.
10. Heilemann, M.; van de Linde, S.; Schuttpelz, M.; Kasper, R.; Seefeldt, B.; Mukherjee, A.; Tinnefeld, P.; Sauer, M. Sub-diffraction-Resolution Fluorescence Imaging with Conventional Fluorescent Probes. *Angew. Chem., Int. Ed.* **2008,** *47*, 6172–6176.
11. Xiong, L. Q.; Chen, Z. G.; Tian, Q. W.; Cao, T. Y.; Xu, C. J.; Li, F. Y. High Contrast Upconversion Luminescence Targeted Imaging *in Vivo* Using Peptide-Labeled Nanophosphors. *Anal. Chem.* **2009,** *81*, 8687–8694.
12. Pandey, S. K.; Gryshuk, A. L.; Sajjad, M.; Zheng, X.; Chen, Y.; Abouzeid, M. M.; Morgan, J.; Charamisinau, I.; Nabi, H. A.; Oseroff, A.;*et al.*Multimodality Agents for Tumor Imaging (PET, Fluorescence) and Photodynamic Therapy. A Possible "See and Treat" Approach. *J. Med. Chem.* **2005,** *48*, 6286–6295.
13. Cai, W.; Chen, K.; Li, Z.; Gambhir, S. S.; Chen, X. Dual-Function Probe for PET and Near-Infrared Fluorescence Imaging of Tumor Vasculature. *J. Nucl. Med.* **2007,** *48*, 1862–1870.
14. Sampath, L.; Kwon, S.; Ke, S.; Wang, W.; Schiff, R.; Mawad, M. E.; Sevick-Muraca1, E. M. Dual-Labeled Trastuzumab-Based Imaging Agent for the Detection of Human Epidermal Growth Factor Receptor 2 Overexpression in Breast Cancer. *J. Nucl. Med.* **2007,** *48*, 1501–1510.
15. Bhushan, K. R.; Misra, P.; Liu, F. B.; Mathur, S.; Lenkinski, R. E.; Frangioni, J. V. Detection of Breast Cancer Microcalcifications Using a Dual-Modality SPECT/NIR Fluorescent Probe. *J. Am. Chem. Soc.* **2008,** *130*, 17648–17649.
16. Ducongé, F.; Pons, T.; Pestourie, C.; Herin, L.; Theze, B.; Gombert, K.; Mahler, B.; Hinnen, F.; Kühnast, B.; Dolle, F.; *et al.*Fluorine-18-Labeled Phospholipid Quantum Dot Micelles for *in Vivo* Multimodal Imaging from Whole Body to Cellular Scales. *Bioconjugate Chem.* **2008,** *19*, 1921–1926.
17. Zheng, J.; Ding, Y.; Tian, B.; Wang, Z.; Zhuang, X. Luminescent and Raman Active Silver Nanoparticles with Polycrystalline Structure. *J. Am. Chem. Soc.* **2008,** *130*, 10472–10473.
18. Kumar, M.; Nyk, R.; Ohulchanskyy, T. Y.; Flask, C. A.; Prasad, P. N. Combined Optical and MR Bioimaging Using Rare Earth Ion Doped NaYF$_4$ Nanocrystals. *Adv. Funct. Mater.* **2009,** *19*, 853–859.
19. Park, Y.; Kim, J. H.; Lee, K. T.; Jeon, K. S.; Na, H. B.; Yu, J. H.; Kim, H. M.; Lee, N.; Choi, S. H.; Aik, S. B.;*et al.*Nonblinking and Nonbleaching Upconverting Nanoparticles as an Optical Imaging Nanoprobe and T1Magnetic Resonance Imaging Contrast Agent. *Adv. Mater.* **2009,** *21*, 4467–4471.
20. Zhou, J.; Sun, Y.; Du, X.; Xiong, L.; Hu, H.; Li, F. Dual-Modality *In Vivo* Imaging Using Rare-Earth Nanocrystals with Near-infrared to Near-infrared (NIR-to-NIR) Upconversion Luminescence and Magnetic Resonance Properties. *Biomaterials* **2010,** *31*, 3287–3295.
21. Stelter, L.; Pinkernelle, J. G.; Michel, R.; Schwartlander, R.; Raschzok, N.; Morgul, M. H.; Koch, M.; Denecke, T.; Ruf, J.; Baumler, H.;*et al.*Modification of Aminosilanized Superparamagnetic Nanoparticles: Feasibility of Multimodal Detection Using 3T MRI, Small Animal PET, and Fluorescence Imaging. *Mol. Imaging Biol.* **2010,** *12*, 25–34.
22. Xie, J.; Chen, K.; Huang, J.; Lee, S.; Wang, J. H.; Gao, J.; Li, X. G.; Chen, X. Y. PET/NIRF/MRI Triple Functional Iron Oxide Nanoparticles. *Biomaterials* **2010,** *31*, 3016–3022.
23. Terreno, E.; Castelli, D. D.; Viale, A.; Aime, S. Challenges for Molecular Magnetic Resonance Imaging. *Chem. Rev.* **2010,** *110*, 3019–3042.
24. Hifumi, H.; Yamaoka, S.; Tanimoto, A.; Citterio, D.; Suzuki, K. Gadolinium-Based Hybrid Nanoparticles as a Positive MR Contrast Agent. *J. Am. Chem. Soc.* **2006,** *128*, 15090–15091.
25. Huang, C. C.; Su, C. H.; Li, W. M.; Liu, T. Y.; Chen, J. H.; Yeh, C. S. Bifunctional Gd$_2$O$_3$/C Nanoshells for MR Imaging and NIR Therapeutic Applications. *Adv. Funct. Mater.* **2009,** *19*, 249–258.

26. Wang, F.; Liu, X. Recent Advances in The Chemistry of Lanthanide-Doped Upconversion Nanocrystals. *Chem. Soc. Rev.* **2009**, *38*, 976–989.

27. Li, F. Y.; Yang, H.; Hu, H. Charpter 13: Luminescent Rare Earth Complexes as Chemosensors and Biological Probes. In *Rare Earth Coordination Chemistry: Fundamentals and Applications*; Huang, C. H., Ed.; Wiley: Singapore, 2010; pp 525–567.

28. Feng, W.; Sun, L. D.; Zhang, Y. W.; Yan, C. H. Synthesis and Assembly of Rare Earth Nanostructures Directed by the Principle of Coordination Chemistry in Solution-Based Process. *Coord. Chem. Rev.* **2010**, *254*, 1038–1053.

29. Wang, F.; Banerjee, D.; Liu, Y. S.; Chen, X. Y.; Liu, X. G. Upconversion Nanoparticles in Biological Labelling, Imaging, and Therapy. *Analyst* **2010**, *135*, 1839–1854.

30. Liu, C.; Lin, J. Rare Earth Fluoride Nano/microcrystals: Synthesis, Surface Modification and Application. *J. Mater. Chem.* **2010**, *20*, 6831–6847.

31. Wang, F.; Han, Y.; Lim, C. S.; Lu, Y.; Wang, J.; Xu, J.; Chen, H.; Zhang, C.; Hong, M.; Liu, X. G. Simultaneous Phase and Size Control of Upconversion Nanocrystals through Lanthanide Doping. *Nature* **2010**, *463*, 1061–1065.

32. Wang, F.; Wang, J.; Liu, X. Direct Evidence of a Surface Quenching Effecton Size-Dependent Luminescence of Upconversion Nanoparticles. *Angew. Chem., Int. Ed.* **2010**, *49*, 7456–7460.

33. Ehlert, O.; Thomann, R.; Darbandi, M.; Nann, T. A Four-Color Colloidal Multiplexing Nanoparticle System. *ACS Nano* **2008**, *2*, 120–124.

34. Wang, X.; Zhuang, J.; Peng, Q.; Li, Y. D. A General Strategy for Nanocrystal Synthesis. *Nature* **2005**, *437*, 121–124.

35. Wang, G. F.; Peng, Q.; Li, Y. D. Upconversion Luminescence of Monodisperse $CaF_2:Yb^{3+}/Er^{3+}$ Nanocrystals. *J. Am. Chem. Soc.* **2009**, *131*, 14200–14201.

36. Liu, Y.; Tu, D.; Zhu, H.; Li, R.; Luo, W.; Chen, X. A Strategy to Achieve Efficient Dual-Mode Luminescence of Eu^{3+} in Lanthanides Doped Multifunctional $NaGdF_4$ Nanocrystals. *Adv. Mater.* **2010**, *22*, 3266–3271.

37. Boyer, J. C.; Vetrone, F.; Cuccia, L. A.; Capobianco, J. A. Synthesis of Colloidal Upconverting $NaYF_4$ Nanocrystals Doped with Er^{3+}, Yb^{3+} and Tm^{3+}, Yb^{3+} via Thermal Decomposition of Lanthanide Trifluoroacetate Precursors. *J. Am. Chem. Soc.* **2006**, *128*, 7444–7445.

38. Chen, D.; Yu, Y.; Huang, F.; Huang, P.; Yang, A.; Wang, Y. Modifying the Size and Shape of Monodisperse Bifunctional Alkaline-Earth Fluoride Nanocrystals through Lanthanide Doping. *J. Am. Chem. Soc.* **2010**, *132*, 9976–9978.

39. Dong, C. H.; van Veggel, F. C. J. M. Cation Exchange in Lanthanide Fluoride Nanoparticles. *ACS Nano* **2009**, *3*, 123–130.

40. Schafer, H.; Ptacek, P.; Eickmeier, H.; Haase, M. Synthesis of Hexagonal Yb^{3+}, Er^{3+}-Doped $NaYF_4$ Nanocrystals at Low Temperature. *Adv. Funct. Mater.* **2009**, *19*, 3091–3097.

41. Li, Z. Q.; Zhang, Y. Monodisperse Silica-Coated Polyvinyl-pyrrolidone/$NaYF_4$ Nanocrystals with Multicolor Upconversion Fluorescence Emission. *Angew. Chem., Int. Ed.* **2006**, *45*, 7732–7735.

42. Nyk, M.; Kumar, R.; Ohulchanskyy, T. Y.; Bergey, E. J.; Prasad, P. N. High Contrast *in Vitro* and *in Vivo* Photoluminescence Bioimaging Using Near Infrared to Near Infrared Upconversion in Tm^{3+} and Yb^{3+} Doped Fluoride Nanophosphors. *Nano Lett.* **2008**, *8*, 3834–3838.

43. Carling, C. J.; Boyer, J. C.; Branda, N. R. Remote-Control Photoswitching Using NIR Light. *J. Am. Chem. Soc.* **2009**, *131*, 10838–10839.

44. Sun, L. N.; Peng, H. S.; Stich, M. I. J.; Achatz, D.; Wolfbeis, O. S. pH Sensor Based on Upconverting Luminescent Lanthanide Nanorods. *Chem. Commun.* **2009**, *33*, 5000–5002.

45. Wu, S. W.; Han, G.; Milliron, D. J.; Aloni, S.; Altoe, V.; Talapin, D. V.; Cohen, B. E.; Schuck, P. J. Non-blinking and Photostable Upconverted Luminescence from Single Lanthanide Doped Nanocrystals. *Proc. Natl. Acad. Sci. U. S. A.* **2009**, *106*, 10917–10921.

46. Wang, M.; Mi, C. C.; Wang, W. X.; Liu, C. H.; Wu, Y. F.; Xu, Z. R.; Mao, C. B.; Xu, S. K. Immunolabeling and NIR-Excited Fluorescent Imaging of HeLa Cells by Using $NaYF_4$:Yb,Er Upconversion Nanoparticles. *ACS Nano* **2009**, *3*, 1580–1586.

47. Mai, H.; Zhang, Y.; Si, R.; Yan, Z.; Sun, L.; You, L.; Yan, C. High-Quality Sodium Rare-Earth Fluoride Nanocrystals: Controlled Synthesis and Optical Properties. *J. Am. Chem. Soc.* **2006**, *128*, 6426–6436.

48. Zhang, P.; Steelant, W.; Kumar, M.; Scholfield, M. Versatile Photosensitizers for Photodynamic Therapy at Infrared Excitation. *J. Am. Chem. Soc.* **2007**, *129*, 4526–4527.

49. Wang, C.; Chen, L.; Liu, Z. Drug Delivery with Upconversion Nanoparticles for Multi-functional Targeted Cancer Cell Imaging and Therapy. *Biomaterials* **2010**, *32*, 1110–1120.

50. Chen, F.; Zhang, S. J.; Bu, W. B.; Liu, X. H.; Chen, Y.; He, Q. J.; Zhu, M.; Zhang, L. X.; Zhou, L. P.; *et al.* A "Neck-Formation" Strategy for an Antiquenching Magnetic/Upconversion Fluorescent Bimodal Cancer Probe. *Chem.—Eur. J.* **2010**, *16*, 11254–11260.

51. Hilderbrand, S. A.; Shao, F.; Salthouse, C.; Mahmood, U.; Weissleder, R. Upconverting Luminescent Nanomaterials: Application to *in Vivo* Bioimaging. *Chem. Commun.* **2009**, *28*, 4188–4190.

52. Kobayashi, H.; Kosaka, N.; Ogawa, M.; Morgan, N. Y.; Smith, P. D.; Murray, C. B.; Ye, X. C.; Collins, J.; Kumar, G. A.; Bell, H.; *et al.* *In Vivo* Multiple Color Lymphatic Imaging Using Upconverting Nanocrystals. *J. Mater. Chem.* **2009**, *19*, 6481–6484.

53. Chen, Z.; Chen, H.; Hu, H.; Yu, M.; Li, F.; Zhang, Q.; Zhou, Z.; Yi, T.; Huang, C. Versatile Synthesis Strategy for Carboxylic Acid-Functionalized Upconverting Nanophosphors as Biological Labels. *J. Am. Chem. Soc.* **2008**, *130*, 3023–3029.

54. Hu, H.; Yu, M.; Li, F.; Chen, Z.; Gao, X.; Xiong, L.; Huang, C. Facile Epoxidation Strategy for Producing Amphiphilic Up-Converting Rare-Earth Nanophosphors as Biological Labels. *Chem. Mater.* **2008**, *20*, 7003–7009.

55. Hu, H.; Xiong, L. Q.; Zhou, J.; Li, F. Y.; Cao, T. Y.; Huang, C. H. Multimodal-Luminescence Core–Shell Nanocomposites for Targeted Imaging of Tumor Cells. *Chem.—Eur. J.* **2009**, *15*, 3577–3584.

56. Xiong, L. Q.; Chen, Z. G.; Yu, M. X.; Li, F. Y.; Liu, C.; Huang, C. H. Synthesis, Characterization, and *in Vivo* Targeted Imaging of Amine-Functionalized Rare-earth Up-converting Nanophosphors. *Biomaterials* **2009**, *30*, 5592–5600.

57. Zhou, J.; Yao, L.; Li, C. Y.; Li, F. Y. A Versatile Fabrication of Upconversion Nanophosphors with Functional-Surface Tunable Ligands. *J. Mater. Chem.* **2010**, *20*, 8078–8085.

58. Xiong, L. Q.; Yang, T. S.; Yang, Y.; Xu, C. J.; Li, F. Y. Long-Term *in Vivo* Biodistribution Imaging and Toxity of Polyacrylic Acid-Coated Upconversion Nanophosphors. *Biomaterials* **2010**, *31*, 7078–7085.

59. Cao, T. Y.; Yang, Y.; Gao, Y.; Zhou, J.; Li, Z. Q.; Li, F. Y. High-Quality Water-Soluble and Surface-Functionalized Upconversion Nanocrystals as Luminescent Probes for Bioimaging, *Biomaterials* 2011, doi:10.1016/j.biomaterials.2010.12.050.

60. Cheng, L.; Yang, K.; Zhang, S.; Shao, M. W.; Lee, S. T.; Liu, Z. Highly-Sensitive Multiplexed in Vivo Imaging Using PEGylated Upconversion Nanoparticles. *Nano Res.* **2010**, *3*, 722–732.

61. Cheng, L.; Yang, K.; Shao, M. W.; Lee, S. T.; Liu, Z. Multicolor In Vivo Imaging of Upconversion Nanoparticles with Emissions Tuned by Luminescence Resonance Energy Transfer. *J. Phys. Chem. C* **2011**, *115*, 2686–2692.

62. Wang, F.; Wang, J.; Liu, X. Direct Evidence of a Surface Quenching Effect on Size-Dependent Luminescence of Upconversion Nanoparticles. *Angew. Chem., Int. Ed.* **2010**, *49*, 7456–7460.

63. Wang, J.; Wang, F.; Xu, J.; Wang, Y.; Liu, Y.; Chen, X.; Chen, H.; Liu, X. Lanthanide-doped $LiYF_4$ Nanoparticles: Synthesis and Multicolor Upconversion Tuning. *C. R. Chim.* **2010**, *13*, 731–736.

64. Wang, F.; Wang, J.; Xu, J.; Xue, X.; Chen, H.; Liu, X. Tunable Upconversion Emissions from Lanthanide-doped

Monodisperse β-NaYF$_4$ Nanoparticles. *Spectrosc. Lett.* **2010,** *43*, 400–405.

65. Roberts, J. E. Lanthanum and Neodymium Salts of Trifluoroacetic Acid. *J. Am. Chem. Soc.* **1961,** *83*, 1087–1088.

66. Sun, Y.; Yu, M. X.; Liang, S.; Zhang, Y. J.; Li, C. G.; Mou, T. T.; Yang, W. J.; Zhang, X. Z.; Li, B. *et al*. Fluorine-18 Labeled Rare-earth Nanomaterials for Positron Emission Tomography Imaging of Sentinel Lymph Node. *Biomaterials* **2011**, *32*, 2999−3007.

67. Zhou, J.; Yu, M. X.; Sun, Y.; Zhang, X. Z.; Zhu, X. J.; Wu, Z. H.; Wu, D. M.; Li, F. Y. Fluorine-18-labeled Gd^{3+}/Yb^{3+}/Er^{3+} codoped NaYF$_4$ nanophosphors for multimodality PET/MR/UCL imaging. *Biomaterials* **2011,** *32*, 1148–1156.